Intrinsic anion diffusivity in lead halide perovskites is facilitated by a soft lattice

Minliang Lai[a,1], Amael Obliger[a,1], Dylan Lu[a,b], Christopher S. Kley[a], Connor G. Bischak[a], Qiao Kong[a], Teng Lei[a], Letian Dou[a,b,c], Naomi S. Ginsberg[a,b,d,e,f], David T. Limmer[a,e,f,2], and Peidong Yang[a,b,e,g,2]

[a]Department of Chemistry, University of California, Berkeley, CA 94720; [b]Materials Sciences Division, Lawrence Berkeley National Laboratory, Berkeley, CA 94720; [c]Davidson School of Chemical Engineering, Purdue University, West Lafayette, IN 47907; [d]Department of Physics, University of California, Berkeley, CA 94720; [e]Kavli Energy NanoScience Institute, Berkeley, CA 94720; [f]Molecular Biophysics and Integrative Bioimaging Division, Lawrence Berkeley National Laboratory, Berkeley, CA 94720; and [g]Department of Materials Science and Engineering, University of California, Berkeley, CA 94720

Contributed by Peidong Yang, October 2, 2018 (sent for review July 26, 2018; reviewed by Qihua Xiong and Xiaoyang Zhu)

Facile ionic transport in lead halide perovskites plays a critical role in device performance. Understanding the microscopic origins of high ionic conductivities has been complicated by indirect measurements and sample microstructural heterogeneities. Here, we report the direct visualization of halide anion interdiffusion in $CsPbCl_3$–$CsPbBr_3$ single crystalline perovskite nanowire heterojunctions using wide-field and confocal photoluminescence measurements. The combination of nanoscale imaging techniques with these single crystalline materials allows us to measure intrinsic anionic lattice diffusivities, free from complications of microscale inhomogeneity. Halide diffusivities were found to be between 10^{-13} and $\sim10^{-12}$ cm^2/second at about 100 °C, which are several orders of magnitudes lower than those reported in polycrystalline thin films. Spatially resolved photoluminescence lifetimes and surface potential measurements provide evidence of the central role of halide vacancies in facilitating ionic diffusion. Vacancy formation free energies computed from molecular simulation are small due to the easily deformable perovskite lattice, accounting for the high equilibrium vacancy concentration. Furthermore, molecular simulations suggest that ionic motion is facilitated by low-frequency lattice modes, resulting in low activation barriers for vacancy-mediated transport. This work elucidates the intrinsic solid-state ion diffusion mechanisms in this class of semisoft materials and offers guidelines for engineering materials with long-term stability in functional devices.

halide perovskite nanowire | anion diffusivity | nanoscale imaging | molecular simulation | soft lattice

Lead halide perovskites are a class of soft ionic crystals with excellent optoelectronic properties ideally suited for photovoltaic and light-emitting applications (1–4). Significant ionic migration has been reported in these materials (5, 6) and is considered to play an important role in anomalous charging hysteresis, light-induced phase segregation, and photoinstability (7–13). The current understanding of ionic transport in lead halide perovskites is based primarily on conventional charge transport studies (14, 15), where the contribution from electrons and comovement of cations and anions is difficult to separate. Furthermore, ionic diffusion has been measured in polycrystalline thin films, replete with grain boundaries where the ion transport is usually faster than in the interior lattice (16), and thus the high ionic conduction reported may not be representative of intrinsic material properties. Although the fast anion-exchange was achieved in cesium lead halide nanocrystals at solid–liquid interfaces (17, 18), high anion diffusivity may not be necessary due to the short solid–solid diffusion path (<10 nm). Therefore, the intrinsic ion diffusion in this class of materials has remained largely unknown.

Traditional solid-state transport characterization techniques provide either direct (e.g., trace diffusion and secondary ion mass spectrometry) or indirect (e.g., nuclear magnetic relaxation and impedance spectroscopy) information of ion diffusion (19). However, most of them only reveal transport properties averaged over macroscopic scales with complications from microstructural heterogeneities. Direct microstructural observation and atomic-scale mechanism of the lattice diffusion are still highly challenging. Recently, well-defined heterostructures of two different halide species in $CsPbX_3$ nanowires were realized through a localized anion exchange reaction (20). The sharp interface with well-defined physical properties (composition, optical, electronic, etc.), controllable geometry, and single crystalline nature make these nanowire heterojunctions ideal platforms to study the intrinsic halide anion interdiffusion. In addition, different halide compositions afford an excellent bandgap tunability with high fluorescence efficiency, which allows for halide anion interdiffusion to be directly monitored by photoluminescence (PL). We combine these measurements with multiscale modeling to elucidate the relationships between mesoscale transport processes and their molecular underpinnings. Together with spatially resolved PL lifetime and surface potential mappings, we further demonstrate how anionic diffusion in lead halides is determined by low barriers to vacancy hopping and facilitated by elastic properties that render the perovskite lattice soft and deformable.

Significance

Understanding and controlling the ion migration in a solid-state semiconductor is essential for device performance in modern photonics, electronics, and optoelectronics. Direct microstructural observation and atomic-scale mechanism of the intrinsic lattice diffusion are still highly challenging. Here, we report the direct visualization of halide anion interdiffusion in $CsPbCl_3$–$CsPbBr_3$ single crystalline nanowire heterojunctions via nanoscale imaging, allowing for the direct measuring of intrinsic lattice diffusivities. The intrinsic halide diffusivities were found to be several orders of magnitudes lower than those reported in polycrystalline thin films. Together with multiscale modeling, we further demonstrate how anionic diffusion in lead halides is determined by low barriers to vacancy hopping and facilitated by the soft perovskite lattice.

Author contributions: M.L., A.O., D.T.L., and P.Y. designed research; M.L., A.O., D.L., C.S.K., C.G.B., Q.K., T.L., and L.D. performed research; M.L., A.O., D.L., C.S.K., D.T.L., and P.Y. analyzed data; and M.L., A.O., N.S.G., D.T.L., and P.Y. wrote the paper.

Reviewers: Q.X., Nanyang Technological University; and X.Z., Columbia University.

The authors declare no conflict of interest.

[1]M.L. and A.O. contributed equally to this work.

[2]To whom correspondence may be addressed. Email: dlimmer@berkeley.edu or p_yang@berkeley.edu.

This article contains supporting information online at www.pnas.org/lookup/suppl/doi:10.1073/pnas.1812718115/-/DCSupplemental.

Published online November 5, 2018.

The $CsPbCl_3$–$CsPbBr_3$ nanowire heterojunctions were synthesized using our previously reported anion exchange chemistry and supported on SiO_2/Si substrates (*SI Appendix*). Heating the nanowires initiated halide anion interdiffusion. The in situ interdiffusion process in the single nanowire was monitored using wide-field PL imaging (Fig. 1*A*). Utilizing a relatively low pump power density and short exposure time, the PL measurement should be negligible to anion interdiffusion. To quantitatively relate the PL emission with Br concentration, we measured the PL spectrum of different uniform $CsPb(Br_xCl_{1-x})_3$ nanowires and the corresponding Br concentration by energy-dispersive X-ray spectroscopy (*SI Appendix*, Figs. S1 and S2). As-synthesized heterojunction nanowires featured a blue/green emission with a clear interface in the PL image (Fig. 1*B*). Two distinct peaks in the wide-field spectrum were observed and identified with the Cl- and Br-rich ends of the nanowire (Fig. 1*C*). The exchange of Br/Cl between the two halide segments induced a time-dependent change of the emission spectrum. After 1.5 h, under a constant temperature of 100 °C, the blue PL peak shifted from 435 to 445 nm, indicating a local change in halide composition, while the green PL peak position remained unchanged (*SI Appendix*, Fig. S3*A*). The PL image taken at that time shows that the interface between the Cl- and Br-rich regions moved in the direction of the Br-rich end (Fig. 1*B*). From 1.5 to 5 h, the blue peak continued to red shift, and its relative intensity to the green peak increased (*SI Appendix*, Fig. S3*B*). With further heating after 5 h, the green peak began to a show a gradual blue shift (*SI Appendix*, Fig. S3*C*), implying Cl diffusion into the Br-rich region. Fig. 1 *F* and *G* shows the PL image and spectrum at 7 h. In solid-state interdiffusion, with concentration-dependent transport coefficients, the equal-molar or Matano plane moves toward the more diffusive species. Furthermore, the slow change of the green emission peak further suggests Cl does not migrate far into the Br end of the wire for times up to 5 h at 100 °C. After 10 h, only one peak in the emission spectrum was present and no interface was evident along the nanowire in the wide-field PL image (Fig. 1 *H* and *I*).

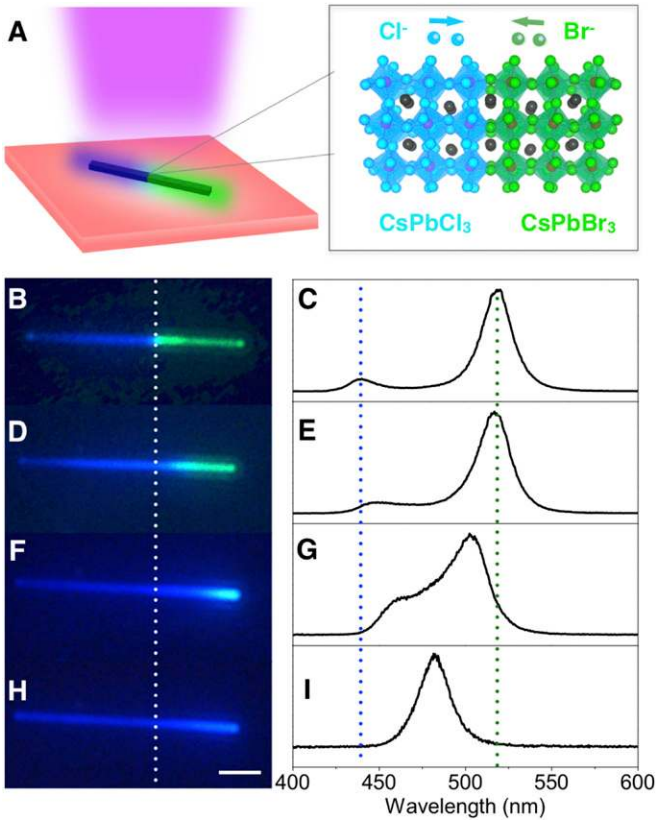

Fig. 1. PL of solid–solid halide anion interdiffusion dynamics. (*A*) Schematics of in situ PL visualization of thermal-driven anion interdiffusion $CsPbCl_3$–$CsPbBr_3$ nanowire. The halide anions (Cl/Br) interdiffuse across the interface at ∼100 °C. The change of Br/Cl ratio in two halide segments would induce the emission wavelength shift; the Br/Cl concentration spatial evolution would be traced by the PL images. PL images and spectrum of $CsPbCl_3$–$CsPbBr_3$ nanowire at initial state (*B* and *C*). After 1.5 h at 100 °C, the green emission (Br-rich) part shrank and the blue emission (Cl-rich) part expanded (*D*). The PL emission of the Br-rich part remained the same, while the Cl-rich emission showed red shift (*E*). After 7 h at 100 °C, the Br-rich part kept shrinking (*F*). The Cl-rich emission kept red shifting and the Br-rich part began blue shifting (*G*). After 10 h at 100 °C, the nanowire showed one-color PL image (*H*) and single peak emission (*I*). (Scale bar: 2 μm.)

Confocal PL resolves the spatial distribution of emissive sites at different wavelengths and can provide higher spatial resolution than conventional wide-field PL. With confocal PL and composition PL tunability in *SI Appendix*, Fig. S2, we could generate a spatial mapping of the local Br concentration along our heterojunction nanowires (*SI Appendix*, Fig. S4). Fig. 2*A* shows the evolution of the bromide concentration profile. After 1.5 h at 100 °C, the Br-rich region shrank by about 1 μm without evolving its composition, which is consistent with the constant green peak observed by in situ PL (Fig. 1 *C* and *E*). The Br concentration in the Cl-rich region increased homogeneously from 0.22 to 0.27. After 5 h, the length of the Br-rich end was about 0.5 μm and the Br concentration in the Cl-rich part continued increasing to 0.38. After 10 h, a smooth concentration profile persisted along the nanowire along with a single peak of the wide-field PL shown in Fig. 1*I*. Confocal PL was also performed to study interdiffusion at different temperatures (*SI Appendix*, Figs. S5 and S6), indicating the same qualitative behavior. At each temperature, the total Br amount across the whole nanowire stayed almost the same, indicating no halide transport into the environment (*SI Appendix*, Fig. S7). Additionally, we also studied the dependence of anion interdiffusion on the sample preparation by fabricating the "reverse" $CsPbCl_3$–$CsPbBr_3$ nanowire heterojunctions, which are created by anion exchange from $CsPbCl_3$ templates. Fig. 2*B* shows the concentration profile evolution for a reverse heterojunction at 125 °C, where the same qualitative behavior was obtained (*SI Appendix*, Fig. S8). Therefore, the heterojunction fabrication process preserves the crystal quality and has no effect on the dynamics of anion interdiffusion. The evolution of concentration profiles strongly suggests a slower anionic diffusion in the Br region, which acts as a "reservoir" for Br. The time needed to deplete the Br-rich part is longer than the time for the Br in the Cl-rich part to distribute homogeneously. Thus, the Br concentration of the whole Cl-rich part increases uniformly in evolution profiles.

To understand the molecular origin of the interdiffusion mechanism, we performed molecular-dynamics (MD) calculations (*SI Appendix*). Previous work has demonstrated that the diffusion of the halide anions is vacancy mediated (7) due to the large formation energies of interstitial defects. To estimate the diffusivity, we computed the free energies to create a vacancy, anion-vacancy exchange rates, and the prefactors associated with the length of the exchange, and its characteristic timescale. This vacancy-mediated process is rendered in Fig. 3 *A*–*C*. We used steered MD (21) with the Jarzynski equality (22) to compute the free energy barriers anions have to overcome to diffuse by exchanging their positions with vacancies. Examples for an equal-molar mixture are shown in Fig. 3*D* for Br and Cl, which exhibit notable asymmetry along the reaction coordinate. This asymmetry arises because vacancies are stabilized by a local enhancement of Br ions, whose correlations decay over two to three unit cells as indicated by the vacancy–halide pair correlation function. An entropic contribution to the barrier accounts

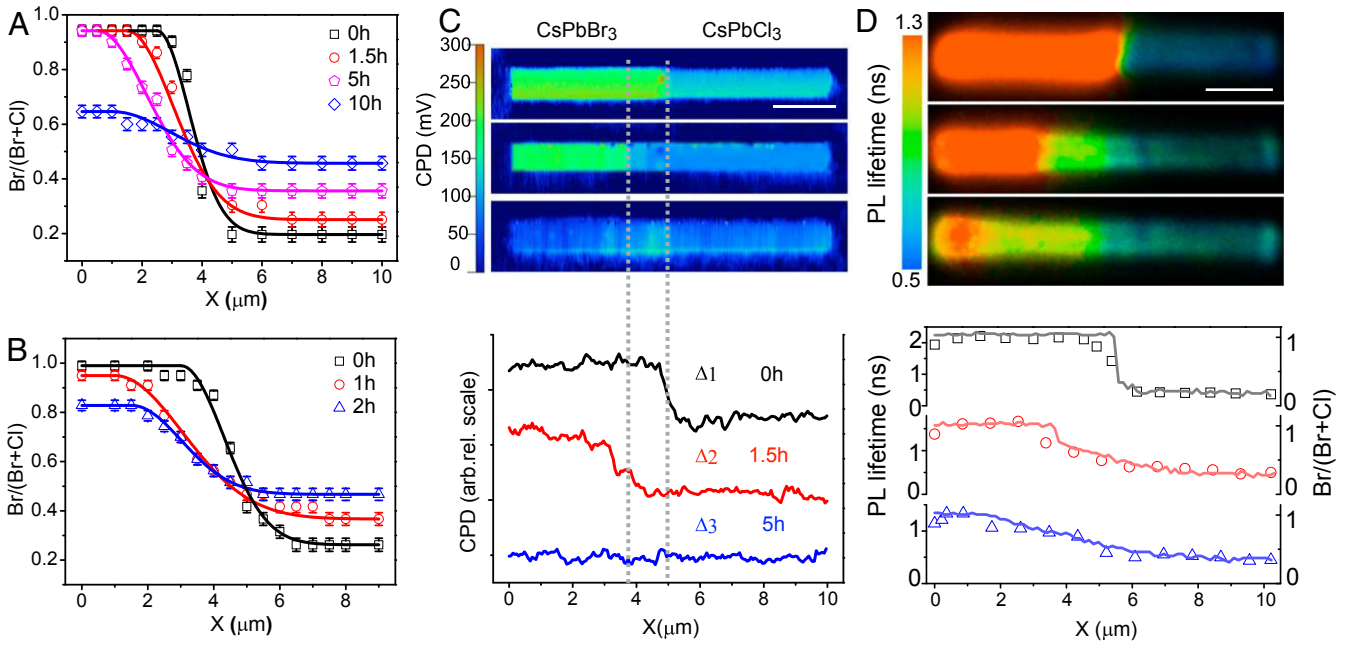

Fig. 2. Concentration profiles, fluorescence lifetime, and electronic structure mapping of anion interdiffusion evolution. (*A*) Br concentration profiles from confocal PL wavelength scan at 100 °C (0 h, black; 1.5 h, red; 5 h, green; 10 h, blue). (*B*) Interdiffusion profiles of reverse heterojunction created from a $CsPbCl_3$ nanowire template at 125 °C (0 h, black; 1 h, red; 2 h, blue). (*C*) The surface potential mapping by Kelvin probe force microscopy (KPFM) of the as-synthesized (*Top*), 1.5 h at 100 °C annealed (*Middle*), and 5 h at 100 °C annealed (*Bottom*) heterojunction nanowire, respectively. (Scale bar: 2 μm.) A distinct surface potential change (Δ_1) ~ 110 meV is observed at the initial $CsPbBr_3$–$CsPbCl_3$ interface. The electronic junction moves ~1.2 μm into the initial $CsPbBr_3$ region with a smaller surface potential change (Δ_2) ~ 100 meV after 1.5 h at 100 °C. Further extending the thermal annealing time to 5 h at 100 °C, the KPFM surface potential maps do not reveal any distinct electronic junction. (*D*) Fluorescence lifetime mapping images of a $CsPbBr_3$–$CsPbCl_3$ nanowire heated for 0 h (*Top*), 1.5 h (*Middle*), and 5 h (*Bottom*) at 100 °C. The axial size of long lifetime component ($CsPbBr_3$ region) becomes shorter after heating, exhibiting a consistent correlation with the evolution of confocal PL images. (Scale bar: 2 μm.) The *Bottom* of *D* shows the PL lifetime profiles with correlated Br/(Br + Cl) profiles. The open dots represent the lifetime distribution along the nanowire, 0 h (black square), 1.5 h (red circle), and 5 h (blue triangle). The solid lines are corresponding Br concentration profiles. The normalized PL lifetime is closely associated with composition evolutions (detail plots in *SI Appendix*, Fig. S12).

for up to one-third of its height. In addition, purely dynamical effects arise due to the slow energy diffusion of the halide perovskite lattice. This is quantified by small values of the transmission coefficient, illustrated in Fig. 3*E*. A significant dynamical correction occurs for all compositions and is largest for the equal-molar mixture (*SI Appendix*). This correction is a result of the weak coupling between the low-frequency octahedral tilting modes that are excited by the hopping vacancy, and the surrounding lattice, and has been noted before as resulting in low thermal conductivities (23) and low photoexcitation cooling rates (24). We have additionally computed the barrier heights for vacancy-mediated transport of Cs, which are 1.25 and 1.4 eV for the pure Br and Cl phases, respectively. These barriers put Cs diffusion on a significantly different timescale compared with anion diffusion. The black line in Fig. 3*F* shows the concentration-dependent hopping rate computed by the Bennet–Chandler procedure, where the hopping rate in the pure Br phase is found to be about three times faster than in the Cl phase. This small difference is insufficient to explain the enhanced diffusion noted in the PL measurements.

Vacancy-mediated diffusion additionally depends on the concentration of vacancies, which is determined by the free energy to form a vacancy in the lattice. Because the lattice is ionic, charge neutrality demands that equilibrium point defects are created in pairs. We used thermodynamic integration to compute the vacancy formation energy of a Schottky defect pair of Cs + X, as a function of composition and temperature. To study the composition dependence, we employed Monte Carlo swapping moves to sample halide compositions. We find from MD calculations that the lattice contribution to the formation free energy is 1.32 and 1.44 eV for Br and Cl, respectively (*SI Appendix*). Together with the appropriate standard state conditions ($\mu_{Br} = -0.9$ eV and $\mu_{Cl} = -1.09$eV) with excess of Cl (*SI Appendix*), the total formation energy is 0.42 and 0.35 eV for Br and Cl, respectively. This results in an equilibrium vacancy concentration of 3×10^{-7} and 2×10^{-9} per unit cell for the pure chloride and bromide phases, respectively, at the conditions considered experimentally in the synthesis of the nanowires (red line in Fig. 3*F*). This equilibrium vacancy concentration is large despite the ionic character of the lattice. This is due to the highly anharmonic lattice with accompanying low-frequency modes and small elastic moduli (25). We find the binding energy of the Schottky defect pairs is below 0.1 eV (*SI Appendix*), on the order of thermal energies, which means that halide ion diffusion is expected to be uncorrelated with cesium diffusion. Therefore, we conclude that it is the enhanced vacancy concentration in the Cl part relative to the Br part that results in the large diffusivity measured experimentally in the Cl region.

To validate the role of the equilibration vacancy concentration along the nanowire, we used Kelvin probe force microscopy (6) to monitor the net flow of vacancies during interdiffusion. Fig. 2*C* shows the 2D surface potential map and corresponding nanowire potential profiles of the as-synthesized (*Top*), 1.5 h at 100 °C annealed (*Middle*), and 5 h at 100 °C annealed (*Bottom*) heterojunction nanowire, respectively. For the as-synthesized heterojunction nanowire, we observe a distinct surface potential change of ~110 meV at the $CsPbBr_3$–$CsPbCl_3$ interface. After 1.5 h at 100 °C, the electronic junction moves about 1.2 μm into the initial $CsPbBr_3$ region with a slightly smaller surface potential change of ~100 meV. The surface potential shows a close correlation with the concentration evolution (*SI Appendix*, Fig. S9). There is no significant surface potential difference

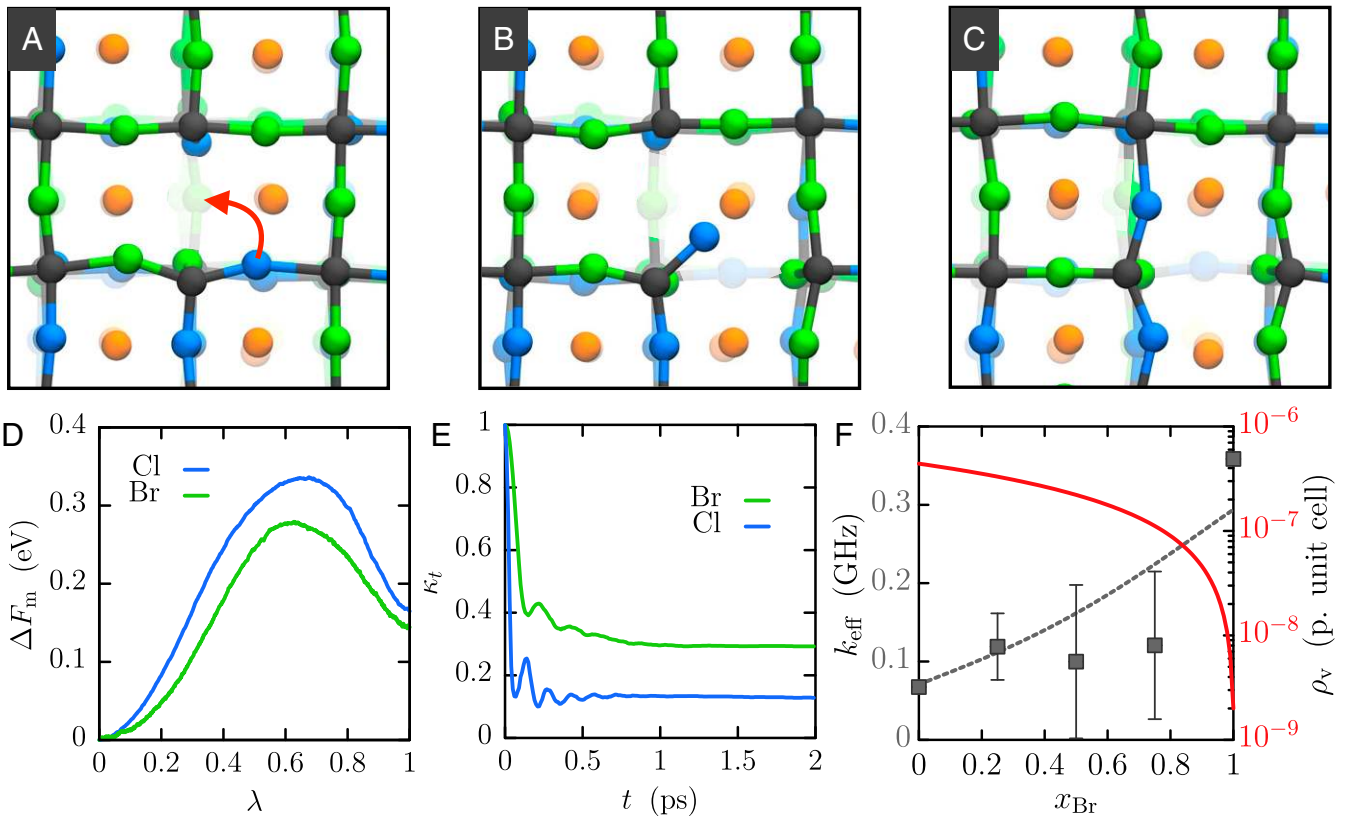

Fig. 3. MD simulation of interdiffusion. (*A*–*C*) Snapshots of a chloride anion swapping with a vacancy in an equal-molar mixture, in the initial position (*A*), on top of the energy barrier (*B*), and in the final position (*C*). Color code: cesium in orange, lead in black, bromide in green, and chloride in blue. The sticks represent the strong lead halide ionic bonds. (*D*) Free energy along halides' trajectories for Cl and Br with given lattice compositions in an equal-molar mixture. $\lambda = (z - z_i)/(z_f - z_i)$ is the dimensionless reaction coordinate, with z the coordinate of the ion. (*E*) Time-dependent transmission coefficient corresponding to the energy barriers shown in *D*. *D* and *E* show results for single trajectories that depend on the local anion composition. Thus, the rates must be averaged over different realizations of the composition. (*F*) Effective hopping rate (gray symbols) corresponding to the interdiffusion coefficient (MD results, 300 K, 1 bar). The dashed line corresponds to the effective rate with linear fits for the Br and Cl rates (*SI Appendix*). The red solid line is the vacancy concentration where the standard-state chemical potentials have been fitted against the experimental interdiffusion coefficients (*SI Appendix*).

throughout the Br- or Cl-rich regions, indicating that a uniform vacancy concentration and a local thermodynamical equilibrium at each region. After 5 h at 100 °C, the surface potential maps do not reveal any distinct electronic junction. No grain boundaries or cracks within the nanowire crystal were observed in the atomic force microscopy images after thermal annealing (*SI Appendix*, Fig. S10). Vacancies generally serve as nonradiative recombination centers with distinct local PL lifetimes (26). We measured local PL lifetimes with fluorescent lifetime imaging microscopy (FLIM) as shown in Fig. 2*D*. The Br-rich region exhibited a longer PL lifetime compared with the Cl-rich part (*SI Appendix*, Fig. S11*A*). The axial size of the long lifetime region becomes shorter after heating (Fig. 2*D*), exhibiting a consistent correlation with the evolution of confocal PL images (*SI Appendix*, Fig. S11 *B* and *C*). As shown in Fig. 2 *C* and *D*, both local PL lifetimes and surface potential show a close dependence on the concentration evolution, suggesting the correlated diffusion of vacancies during interdiffusion. These two measurements qualitatively indicate that the vacancy concentration is locally at equilibrium and depends only on the Br concentration.

A constant interdiffusion coefficient D may be estimated by the average diffusion length $L \cong 2\sqrt{Dt}$ for an ideal semiinfinite model (27). The interdiffusion length is around 1~2.5 μm after 1.5 h of constant heating, resulting in interdiffusion coefficient around 10^{-13}~10^{-12} cm^2/s at 75–125 °C. The evolution of the concentration profiles during interdiffusion measured from confocal PL can be exploited to calculate the interdiffusion coefficient as a function of the Br concentration. In principle, this transport coefficient depends on the hopping rates of Cs, Br, and Cl, as well as geometrical factors and the relative activities of

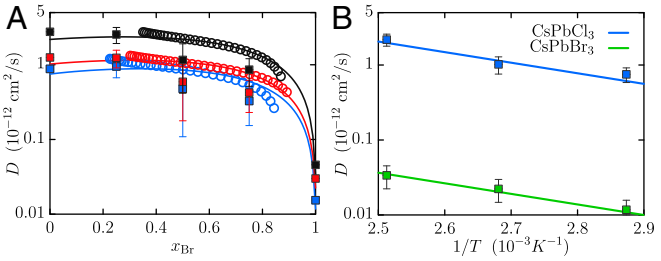

Fig. 4. Concentration-dependent interdiffusivity. (*A*) Experimental interdiffusion coefficient at different temperatures as function of Br concentration by Boltzmann–Matano method at 125 °C (black circles), 100 °C (red circles), and 75 °C (blue circles). The solid lines correspond to the theoretical model fitted against experimental data (*SI Appendix*), which lead to the vacancy concentration shown by Fig. 3*F*. The solid squares are interdiffusion coefficients from molecular simulations where the vacancy concentration is given by Fig. 3*F*. (*B*) Intrinsic diffusion coefficients of pure $CsPbBr_3$ (green) and $CsPbCl_3$ (blue) as a function of inverse temperature. The diffusion coefficients of the pure phases are obtained by extrapolation of the experimental data via the theoretical model. The solid lines stand for the exponential fits $D = D_0 e^{-E/k_B T}$. The activation energy of anion diffusion is 0.28 eV for both $CsPbBr_3$ and $CsPbCl_3$.

the vacancies in the two phases. However, the simulation results suggest that the vacancies are dilute, the Cs-halide Schottky pairs are unbound, and the hopping rates of both anions are nearly the same and are orders of magnitude larger than the analogous cation hopping rate. Under these assumptions, anion interdiffusion can be regarded as decoupled from Cs migration, and the corresponding coefficient $D(c)$ fully characterizes the dynamics (28). Fick's second law gives the evolution of the Br concentration, c, at a time t and with spatial coordinate x, and with concentration-dependent interdiffusion coefficient $D(c)$ as follows:

$$\frac{\partial c}{\partial t} = D(c)\frac{\partial^2 c}{\partial x^2} + \frac{\mathrm{d}D(c)}{\mathrm{d}x}\left(\frac{\partial c}{\partial x}\right). \quad [1]$$

We use the classical Boltzmann–Matano method to extract $D(c)$ from the concentration profiles, shown in *SI Appendix*, Fig. S13 (29–31). Our experimental estimates of the interdiffusion coefficient are shown as function of the bromide concentration and the temperature in Fig. 4*A*. Since the Boltzmann–Matano method is sensitive to the boundary conditions of the Br concentration profiles (*SI Appendix*, Fig. S14), the calculated interdiffusion coefficient in *SI Appendix*, Fig. S15 shows a decreasing trend for the concentration profiles of the longer annealing time. The "reverse" nanowire heterojunction has similar diffusion coefficients in *SI Appendix*, Fig. S15*C* to the "forward" $CsPbCl_3$–$CsPbBr_3$ nanowire at 125 °C, which quantitatively confirms insignificant effects of the preparation of heterojunctions on anion interdiffusion.

Following Belova and Murch (28), when the anion rates are larger than the cesium rate (k_{Br}, $k_{Cl} \gg k_{Cs}$), the interdiffusion coefficient can be further expressed as function of the Br concentration c in a simple way:

$$D(c) = a(c)^2 \rho_v(c) k_{\mathrm{eff}}(c), \quad [2]$$

where a, ρ_v, and k_{eff} are the lattice spacing, the vacancy concentration per unit cell, and an effective rate that depends on the Br and Cl rates via a specific mixing rule (*SI Appendix*). Here, we have considered the crystal $CsPbBr_xCl_{3-x}$ as an ideal solid solution since the halide anions are randomly distributed throughout the lattice. We should emphasize that, in our case, the interdiffusivity is a direct measure of the off-diagonal Onsager coefficient correlating the diffusion of Br and Cl (28). In addition, the intrinsic diffusivities of the anions are the same and are equal to the interdiffusion coefficient. Despite an increasing hopping rate with the Br fraction (black line in Fig. 3*F*), $CsPbCl_3$ has a higher interdiffusivity than $CsPbBr_3$, owing to a higher vacancy concentration that dominates interdiffusion. Each quantity entering Eq. **2** is obtained by MD, but the experimental vacancy concentration also depends on the synthesis conditions through the standard-state chemical potentials for the pure Br and Cl phases (*SI Appendix*). Therefore, combining the experimental and MD interdiffusion coefficients (Fig. 4*A*) gives us the standard states and thus the vacancy concentration (red line in Fig. 3*F*). We found activation energies for both pure phases to be 0.28 eV by fitting the diffusion coefficients of pure $CsPbBr_3$ and $CsPbCl_3$ as a function of temperature with an Arrhenius law (Fig. 4*B*). This activation energy slightly differs from the one directly computed from MD simulations (0.3 eV) because the small differences of the fitted standard states at different temperatures add a contribution to the activation energy. This result is close to the value reported by Koscher et al. (32) (0.33 eV) from anion exchange in nanocrystals but lower than that by Pan et al. (33) (0.44 eV) found from interdiffusion experiments in nanowires. Comparing to polycrystalline thin films, our results clearly show low interdiffusion coefficients. The high grain boundary diffusivity can be attributed to high defect density and disordered interfaces of polycrystals, as evidenced by Huang and coworkers (6), who showed a lower ion migration in larger grain size perovskite thin films. By eliminating grain boundaries and other extended defects in the single-crystal nanowires, our study has clarified a lower intrinsic anion diffusivity in lead halide perovskites. This finding suggests improving crystallization processes and reducing grain boundaries might be an effective approach to enhance the long-term stability of these materials in real devices.

We have developed a robust combination of experimental and numerical techniques to unravel halide migration during interdiffusion in lead halide perovskites. Additional surface/interface processes may involve with anion interdiffusion, such as interfacial strain, surface defect, doping level change (carrier concentration), the band structure alignment, built-in electrical field, etc. The unique properties of $CsPbX_3$ make these materials invaluable to show the strength of the theory of solid-state diffusion. Similarly, the cation diffusion dynamics can be further investigated in other heterosystems with two different cation species, such as $CsPbBr_3$–$CsSnBr_3$ and $CsPbBr_3$–$FAPbBr_3$. This work elucidates the intrinsic solid-state ion diffusion mechanisms in this class of soft materials. The clear picture of ion diffusion dynamics may enable the precise tailoring of ion transport properties combining with defect chemistry at microscopic, even atomic, scales, which stimulates a direction to extensive nanoionic and optoionic applications in halide perovskites.

Materials and Methods

Additional details regarding the materials and methods may be found in *SI Appendix*.

PL Measurements. PL measurements were performed using OBIS 375 nm LX 50-mW laser. The full intensity of the beam is 1 mW. Using an iris diaphragm and a focusing lens, a Gaussian beam spot with a waist of ~30 μm was obtained. The output power of the excitation source was adjusted by neutral density filters (normally 0.001~1 mW). Emission from nanowires was collected with a bright-field microscope objective (Nikon 50×, N.A. 0.55, in a Nikon ME600 optical microscope) and routed via optical fibers to a UV-vis spectroscopy spectrometer (Princeton Instruments/Acton) equipped with a 1,200 groove/mm grating blazed at 300 nm and a liquid N_2-cooled CCD. A layer of poly(methyl methacrylate) (PMMA) was coated on the sample in a glovebox, and then put in vacuum for about 10 min for solidification. The PMMA layer can protect the perovskite samples from the air during the heating. For in situ PL measurements, a heating stage (INSTEC STC200) was coupled to the wide-field PL setup. The heating stage takes about 5~10 min to reach the setting temperature. We used relatively low power density (about 1~100 W/cm^2) for the PL measurements. The sample was kept in the dark during the heating process except for a very short exposure time (a few seconds) to the laser beam during the PL collection. Considering a low pump power density and very short laser exposure time compared with the long annealing time, the light effect should be negligible to anion interdiffusion. The PL images were taken using a Zeiss Axio Scope.

Confocal PL Mapping. Confocal PL mapping was performed using a Carl Zeiss LSM710 confocal microscope, using a 20×, 0.8 N.A. objective and a 405-nm laser excitation source. All images were collected with the default optimal setting for *XY* pixels and scanning time from Zen2010 software. Lambda scans were performed by collecting a series of images while scanning the emission grating in 5-nm spectral windows to vary the collected wavelength range. To get high spatial resolution, 1-AU pinhole was applied and the gain was tuned accordingly to get optimized signal. The confocal PL images were lambda-coded with Zen2010 software. The samples were coated with PMMA. The measurements were performed at room temperature after being heated in a glovebox for a certain time.

FLIM Measurements. SiO_2/Si substrates with $CsPbCl_3$–$CsPbBr_3$ nanowire heterojunctions are attached on glass slides for the measurements using a 50×, 0.55 N.A. air objective by a LSM 510 NLO AxioVert200M confocal laser-scanning microscope equipped with a Mai-Tai HP tunable laser. The excitation wavelength is 405 nm, which is from the second harmonic of 810 nm (<100 fs, 80 MHz). Lifetime measurements were performed using Becker-Hickl SPC-150 time-correlated single-photon counting. The electrical time resolution is 6.6-ps fwhm, 2.5-ps rms. The lifetime decay is collected and

analysis using Becker-Hickl SPCM software. The samples were coated with PMMA and heated in a glovebox for a certain time before the measurement at room temperature.

ACKNOWLEDGMENTS. We thank Dr. Jia Lin for helpful discussion. We thank Holly Aaron and Jen-Yi Lee for their microscopy training and assistance. This work was supported by the US Department of Energy, Office of Science, Office of Basic Energy Sciences, Materials Sciences and Engineering Division, under Contract DE-AC02-05-CH11231 within the Physical Chemistry of Inorganic Nanostructures Program (KC3103). This research used resources of the National Energy Research Scientific Computing Center, a US Department of Energy Office of Science User Facility operated under Contract DE-AC02-05CH11231. M.L., Q.K., and T.L. thank the fellowship support from Suzhou Industrial Park. C.S.K. acknowledges support by the Alexander von Humboldt Foundation. C.G.B. acknowledges a National Science Foundation (NSF) Graduate Research Fellowship (DGE 1106400), and N.S.G. acknowledges a Packard Fellowship for Science and Engineering, a Camile Dreyfus Teacher-Scholar Award, and an Alfred P. Sloan Research Fellowship. The FLIM experiments were conducted at the Cancer Research Laboratory Molecular Imaging Center, University of California, Berkeley, which was supported by NSF Grant DBI-0116016. The LSM 710 confocal microscopic experiments were conducted at The College of Natural Resources Biological Imaging Facility, University of California, Berkeley, which was supported in part by National Institutes of Health S10 Program under Award 1S10RR026866-01. The content is solely the responsibility of the authors and does not necessarily represent the official views of the National Institutes of Health.

1. Burschka J, et al. (2013) Sequential deposition as a route to high-performance perovskite-sensitized solar cells. *Nature* 499:316–319.
2. Lee MM, Teuscher J, Miyasaka T, Murakami TN, Snaith HJ (2012) Efficient hybrid solar cells based on meso-superstructured organometal halide perovskites. *Science* 338:643–647.
3. Dou L, et al. (2015) Atomically thin two-dimensional organic-inorganic hybrid perovskites. *Science* 349:1518–1521.
4. Liu D, Kelly TL (2014) Perovskite solar cells with a planar heterojunction structure prepared using room-temperature solution processing techniques. *Nat Photonics* 8: 133–138.
5. Haruyama J, Sodeyama K, Han L, Tateyama Y (2015) First-principles study of ion diffusion in perovskite solar cell sensitizers. *J Am Chem Soc* 137:10048–10051.
6. Xiao Z, et al. (2015) Giant switchable photovoltaic effect in organometal trihalide perovskite devices. *Nat Mater* 14:193–198.
7. Eames C, et al. (2015) Ionic transport in hybrid lead iodide perovskite solar cells. *Nat Commun* 6:7497.
8. Gratia P, et al. (2016) Intrinsic halide segregation at nanometer scale determines the high efficiency of mixed cation/mixed halide perovskite solar cells. *J Am Chem Soc* 138:15821–15824.
9. Hoke ET, et al. (2015) Reversible photo-induced trap formation in mixed-halide hybrid perovskites for photovoltaics. *Chem Sci (Camb)* 6:613–617.
10. Meloni S, et al. (2016) Ionic polarization-induced current-voltage hysteresis in CH3NH3PbX3 perovskite solar cells. *Nat Commun* 7:10334.
11. Miyano K, Yanagida M, Tripathi N, Shirai Y (2016) Hysteresis, stability, and ion migration in lead halide perovskite photovoltaics. *J Phys Chem Lett* 7:2240–2245.
12. Snaith HJ, et al. (2014) Anomalous hysteresis in perovskite solar cells. *J Phys Chem Lett* 5:1511–1515.
13. Bischak CG, et al. (2017) Origin of reversible photoinduced phase separation in hybrid perovskites. *Nano Lett* 17:1028–1033.
14. Mizusaki J, Arai K, Fueki K (1983) Ionic conduction of the perovskite-type halides. *Solid State Ion* 11:203–211.
15. Yang TY, Gregori G, Pellet N, Grätzel M, Maier J (2015) The significance of ion conduction in a hybrid organic-inorganic lead-iodide-based perovskite photosensitizer. *Angew Chem Int Ed Engl* 54:7905–7910.
16. Fisher JC (1951) Calculation of diffusion penetration curves for surface and grain boundary diffusion. *J Appl Phys* 22:74–77.
17. Zhang D, et al. (2016) Synthesis of composition tunable and highly luminescent cesium lead halide nanowires through anion-exchange reactions. *J Am Chem Soc* 138:7236–7239.
18. Akkerman QA, et al. (2015) Tuning the optical properties of cesium lead halide perovskite nanocrystals by anion exchange reactions. *J Am Chem Soc* 137:10276–10281.
19. Shewmon P (2016) *Diffusion in Solids* (Springer, Berlin).
20. Dou L, et al. (2017) Spatially resolved multicolor $CsPbX_3$ nanowire heterojunctions via anion exchange. *Proc Natl Acad Sci USA* 114:7216–7221.
21. Park S, Khalili-Araghi F, Tajkhorshid E, Schulten K (2003) Free energy calculation from steered molecular dynamics simulations using Jarzynski's equality. *J Chem Phys* 119: 3559–3566.
22. Jarzynski C (1997) Nonequilibrium equality for free energy differences. *Phys Rev Lett* 78:2690.
23. Lee W, et al. (2017) Ultralow thermal conductivity in all-inorganic halide perovskites. *Proc Natl Acad Sci USA* 114:8693–8697.
24. Monahan DM, et al. (2017) Room-temperature coherent optical phonon in 2D electronic spectra of $CH_3NH_3PbI_3$ perovskite as a possible cooling bottleneck. *J Phys Chem Lett* 8:3211–3215.
25. Mishin Y, S⊘rensen MR, Voter AF (2001) Calculation of point-defect entropy in metals. *Philos Mag A* 81:2591–2612.
26. deQuilettes DW, et al. (2015) Solar cells. Impact of microstructure on local carrier lifetime in perovskite solar cells. *Science* 348:683–686.
27. Shewmon NT, Yu H, Constantinou I, Klump E, So F (2016) Formation of perovskite heterostructures by ion exchange. *ACS Appl Mater Interfaces* 8:33273–33279.
28. Belova IV, Murch GE (2004) Analysis of interdiffusion via vacancy-pairs in strongly ionic solids. *Philos Mag* 84:3637–3653.
29. Jones J, Cutler IB (1971) Interdiffusion in the system MnxO-MgO. *J Am Ceram Soc* 54: 335–338.
30. Lupascu A, Kevorkian A, Boudet T, Persegol D, Levy M (1996) Modeling ion exchange in glass with concentration-dependent diffusion coefficients and mobilities. *Opt Eng* 35:1603–1610.
31. Matano C (1933) On the relation between the diffusion-coefficients and concentrations of solid metals (the nickel-copper system). *Jpn J Appl Phys* 8:109–113.
32. Koscher BA, Bronstein ND, Olshansky JH, Bekenstein Y, Alivisatos AP (2016) Surface- vs diffusion-limited mechanisms of anion exchange in $CsPbBr_3$ nanocrystal cubes revealed through kinetic studies. *J Am Chem Soc* 138:12065–12068.
33. Pan D, et al. (2018) Visualization and studies of ion-diffusion kinetics in cesium lead bromide perovskite nanowires. *Nano Lett* 18:1807–1813.